

ARTICLE

Open Access

Real picture of magnetic domain dynamics along the magnetic hysteresis curve inside an advanced permanent magnet

Makoto Takeuchi¹, Motohiro Suzuki^{1,2,3}, Shintaro Kobayashi^{3,4}, Yoshinori Kotani³, Tetsuya Nakamura^{3,4,5}, Nobuaki Kikuchi^{1,6}, Anton Bolyachkin⁴, Hossein Sepehri-Amin⁴, Tadakatsu Ohkubo⁴, Kazuhiro Hono⁴, Yasuhiro Une⁷ and Satoshi Okamoto^{1,4,6}

Abstract

In the long history of permanent magnet research for more than 100 years, three-dimensional magnetic microscopy has been eagerly awaited to elucidate the origin of the magnetic hysteresis of permanent magnets. In this study, we succeeded in observing the three-dimensional magnetic domain structure of an advanced high-coercivity Nd-Fe-B-based permanent magnet throughout the magnetic hysteresis curve using a recently developed hard X-ray magnetic tomography technique. Focused-ion-beam-based three-dimensional scanning electron microscopy was employed to study the relationship between the observed magnetic domains and the microstructure of the magnet for the same observing volume. Thermally demagnetized and coercivity states exhibit considerably different magnetic domain structures but show the same periodicity of $2.3\text{ }\mu\text{m}$, indicating that the characteristic length of the magnetic domain is independent of the magnetization states. Further careful examination revealed some unexpected magnetic domain behaviors, such as running perpendicular to the magnetic easy axis and reversing back against the magnetic field. These findings demonstrate a wide variety of real magnetic domain behaviors along the magnetic hysteresis inside a permanent magnet.

Introduction

Magnetic hysteresis is a fundamental function of permanent magnets. The development of permanent magnets, which has a long history since the investigation of KS steel in 1917¹, can be expressed as the technological effort to enlarge the magnetic hysteresis loop^{2–6}. The magnetic hysteresis of permanent magnets is mainly characterized by the factors of high saturation magnetization, high remanent magnetization, large coercivity, and good squareness. Among them, only the saturation magnetization is an intrinsic property of the material; the others are related to magnetization reversal

processes that largely depend on the microstructure of the magnets^{5,6}. These characteristics are the macroscopic consequences of numerous microscopic magnetic domain nucleations and displacements inside magnet bodies. Therefore, magnetic domain observations are critical for permanent magnet studies.

Although magnetic domain observations of permanent magnets have been studied extensively using various techniques, such as magneto-optical Kerr effect (MOKE) microscopy, Lorentz transmission electron microscopy, and hard or soft X-ray magnetic circular dichroism (XMCD) microscopy^{7–17}, all these techniques are limited to observations of magnetic domains on surfaces and thin films. Owing to the presence of a surface demagnetization field and surface defects, the surface magnetic domain structure does not reflect the real magnetic domain structure within a magnet body. Moreover, most conventional magnetic domain

Correspondence: Motohiro Suzuki (m-suzuki@kwansei.ac.jp) or Satoshi Okamoto (satoshi.okamoto.c1@tohoku.ac.jp)

¹Institute of Multidisciplinary Research for Advanced Materials (IMRAM), Tohoku University, Sendai 980-8577, Japan

²Kwansei Gakuin University, Sanda 669-1330, Japan

Full list of author information is available at the end of the article

observation techniques, such as MOKE microscopy, require mirror-polished surfaces. The polishing process significantly alters intrinsic magnetic properties such as the magneto-crystalline anisotropy of the surface, which prevents researchers from observing the real magnetic domain structure that governs the hysteresis loops of bulk magnets.

Until recently, micromagnetic simulation was the only method utilized to study the magnetic domain structure inside a magnet body. Furthermore, variations in the magnetic domain structure along the magnetic hysteresis have been calculated for various microstructure models of permanent magnets^{18–22}. However, even using modern computation environments, the maximum size of the calculation models has been limited to several hundred cubic nanometers, which is orders of magnitude smaller than the single grain size of a real permanent magnet^{19–21}. This limitation is attributed to the need for the cell size of the calculation model to be smaller than the exchange length of the permanent magnet on the order of nanometers, i.e., ~4 nm for Nd₂Fe₁₄B. A 1/100 or 1/1000 scale model was adopted to emulate the microstructure of a real permanent magnet. Compared with a real permanent magnet, the calculated coercivity of the model tends to be much larger than the experimental coercivity due to the limited model size and the lack of complexity. Recently, a model size of ~2 μm with a sufficiently large distribution of grain orientation was reported to reproduce experimental magnetization curves²².

The attempt to experimentally observe the magnetic domain structure inside a magnet body was first demonstrated by magnetic tomography measurements of a soft magnetic Fe-Si rod (8 mm in diameter) with a neutron beam²³. Neutrons are suitable for magnetic tomography measurements of bulk magnets because of their sufficiently long penetration depth in magnetic materials. However, neutron magnetic tomography cannot be applied to permanent magnet studies because the 35 μm spatial resolution is considerably larger than the typical magnetic domain size of permanent magnets. Recently, magnetic tomography measurements with soft X-ray²⁴ and hard X-ray^{25–29} beams have been reported. For these X-ray techniques, a spatial resolution on the order of 100 nm or less is available. The application of soft X-ray magnetic tomography is limited to magnetic thin films because the penetration depth of a soft X-ray beam is on the order of 100 nm²⁴. In contrast, a hard X-ray beam has a moderate penetration depth on the order of micrometers. Furthermore, using a circularly polarized hard X-ray beam, magnetic imaging based on XMCD microscopy is possible for noble metals and rare earth elements¹⁶, which are essential elements for hard magnetic materials. Thus, hard X-ray magnetic tomography is considered to be a suitable approach for the three-dimensional (3D) magnetic domain observations of bulk

permanent magnets. However, this approach has one technical issue that must be addressed. Most previous reports of hard X-ray magnetic tomography studied the 3D distribution of vector or scalar magnetization components in soft-magnetic Gd-Fe(Co) alloys at zero or a very weak external magnetic field^{25–27}. Although the X-ray magnetic tomography measurement of a single grain of a Nd-Fe-B permanent magnet with a diameter of 6 μm was reported, this was performed in a thermally demagnetized state without applying an external magnetic field²⁸. In a more recent study, hard X-ray magnetic tomography measurements with a moderate magnetic field (~0.5 T) were reported²⁹. The magnetic field strength in this study was insufficient to investigate permanent magnets. To perform X-ray tomography measurements of permanent magnets along the magnetic hysteresis curve, a large electro- or superconducting magnet, with a magnetic field of several Tesla, needs to be combined with the X-ray tomography setup; such an experimental system is technically challenging to construct.

In this study, we performed hard X-ray magnetic tomography measurements in an advanced high-coercivity Nd-Fe-B sintered magnet along the magnetic hysteresis curve using separately equipped electro- and superconducting magnets. By varying the magnetic field from +5.5 T to -5.5 T, we successfully visualized the actual magnetic domain dynamics of a Nd-Fe-B-based permanent magnet along its magnetic hysteresis, that is, the nucleation of reversed domains followed by the expansion of domains with domain wall displacements. Scanning electron microtomography was employed for the same observing volume to elucidate the correlation between the 3D magnetic domain structure and the microstructure of the Nd-Fe-B magnet. Consequently, some unexpected behaviors of the local magnetization reversals were observed.

Materials and methods

Nd-Fe-B magnet

Nd-Fe-B magnets originally invented in 1982^{30,31} have been widely used as the highest-performance permanent magnets^{5,6}. Recently, Nd-Fe-B magnets have gained further significance because they are indispensable for high-energy-efficiency motors and generators³². The advanced Nd-Fe-B magnet used in this study consists of unprecedentedly fine Nd₂Fe₁₄B grains with very high coercivity compared with conventional Nd-Fe-B sintered magnets^{33–35} (see Supplementary S1 and Supplementary Fig. S1). The fine-grained Nd-Fe-B sintered magnet was prepared using a pressless sintering process (PLP) with He-jet milled Ga-doped Nd-Fe-B powder^{36,37}. The average diameter of the Nd-Fe-B alloy powder was 1.2 μm, and the composition was Nd_{23.2}Pr_{7.39}Co_{0.89}Al_{0.21}Cu_{0.04}Ga_{0.29}B_{0.86}Fe_{bal} in wt. %. The grain boundary modification process using a Tb₇₀Cu₃₀ eutectic alloy further improved the coercivity³⁸. After the

grain boundary diffusion process at 860 °C for 10 h and subsequent annealing at 460 °C for 1.5 h, the coercivity reached as large as 2.7 T at ambient temperature.

Micropillar of the Nd-Fe-B magnet

The micropillar of the Nd-Fe-B magnet was fabricated using a focused ion beam (FIB) technique with Ga ions. The acceleration voltage was varied from 30 kV for rough shaping up to a 30 μm target width to 5 kV for a final target width of 18 μm to minimize the FIB damage on the magnetic properties of the micropillar sample. After the FIB process, a 10-nm-thick Ta film was deposited on the pillar surface as an oxidation protection layer.

X-ray scalar magnetic tomography measurements combined with strong magnetic fields

X-ray scalar magnetic tomography measurements were performed at BL39XU of SPring-8 using a previously reported setup²⁶. Circularly polarized monochromatic hard X-ray radiation was generated using a Si 111 double-crystal monochromator and a 0.45-mm-thick diamond phase retarder. The X-ray beam was then microfocused to a spot with dimensions of 100 (horizontal) × 130 (vertical) nm² in full width at half maximum (FWHM) at the sample position. The X-ray energy was tuned to 6.726 keV, where the X-ray magnetic circular dichroism signal takes a maximum at the Nd L_2 edge. A micropillar PLP magnet sample was mounted on high-precision stages with x - z translations and rotation θ about the vertical (z) direction. Polarization-averaged X-ray absorption (XAS) projection images, $\mu(X, Z, \theta) = (\mu^+ + \mu^-)/2$, were taken by two-dimensionally scanning the sample in the x - z plane, which is perpendicular to the incident X-ray beam with sampling steps of 100 nm in both the x and z directions. Here, $\mu^+ = \int \mu_i^+(x \cos \theta - y \sin \theta, x \sin \theta + y \cos \theta) dy$ [$\mu^- = \int \mu_i^-(x \cos \theta - y \sin \theta, x \sin \theta + y \cos \theta) dy$] represents the X-ray absorption for the right (left) circular polarization integrated along the X-ray beam direction (y). The magnetic projection images, $\Delta\mu(x, z, \theta) = \mu^+ - \mu^-$, were recorded simultaneously by monitoring the XMCD signals using a lock-in amplifier locked to an X-ray helicity modulation frequency of 37 Hz. The XAS and XMCD projection images were collected at sample rotation angles of $-90^\circ \leq \theta \leq 85^\circ$ with a step of 5° (see Supplementary S3 and Supplementary Fig. S3a). The projection image area was 32 μm (x) × 10 μm (z) to cover the region of interest with a height of 10 μm and 15 μm below the tip of the pillar, as indicated in yellow in Fig. 1a. The acquisition time for obtaining the full tomographic data was 11 h.

We used a separate setup of an electromagnet and a superconducting magnet elsewhere in the facility to apply a strong magnetic field to the sample. The sample holder was

detached from the X-ray tomography setup and transferred to an external electromagnet (maximum field of 2.8 T) or superconducting magnet (8 T) when applying a magnetic field. The sample holder was reattached to the X-ray apparatus after the application of the magnetic field. X-ray tomography measurements were performed for the magnetic remanent state of the sample at zero field. This procedure was repeated while varying the magnetic field from 5.5 T (positive saturation) to -5.5 T (negative saturation). Thus, all the magnetic tomography data in this study are for the remanent state along the demagnetizing process. Reproducibility in the sample position was within ±3 μm using a kinematic sample holder mount (see Supplementary S2 and Supplementary Fig. S2a), allowing for smooth sample reattachment and reliable data acquisition. High stability of the experimental environment was ensured during the measurements (see Supplementary S2 and Supplementary Fig. S2b).

Reconstruction of three-dimensional magnetic images

The standard algorithm of the algebraic reconstruction technique (ART) was applied to 36 projection images collected at angles from -90° to +85° with a step of 5° for reconstructing three-dimensional (3D) XAS images. For the reconstruction of 3D magnetic images, a modified ART algorithm was applied to the measured XMCD projections. Among the components of the magnetization vector, $\mathbf{m}(x, y, z) = (m_x, m_y, m_z)$, where m_y is the only component parallel to the easy magnetization axis and is assumed to have a finite value. The m_x and m_z components are zero because of the strong uniaxial anisotropy of the hard magnet considered in this study. Therefore, we modified the ART algorithm to consider the $\cos\theta$ factor added in the standard Radon transformation that appears in this restricted case of XMCD projections as $\Delta\mu(x, z, \theta) \propto \int m_y \cos\theta dy$. The spatial resolution of the reconstructed 3D magnetic image was estimated to be 360 nm²⁶. The tomographic reconstructions were performed using house-made macros running on Igor Pro 8 (<https://www.wavemetrics.com/products/igorpro>). ImageJ (<https://imagej.nih.gov/ij/>) software was used to render the 3D representations and generate movies.

Scanning electron microtomography

Microtomography was performed after the magnetic tomography measurement. Serial backscattered electron SEM images of the (x - y) plane were obtained by slicing the micropillar with a 50 nm step using an FIB with Ga ions.

3D fast Fourier transformation

Fast Fourier transformation (FFT) was applied to the reconstructed 3D magnetic image data to obtain the 3D Fourier transform spectrum of a magnetic image. The central part of the reconstructed magnetic image that

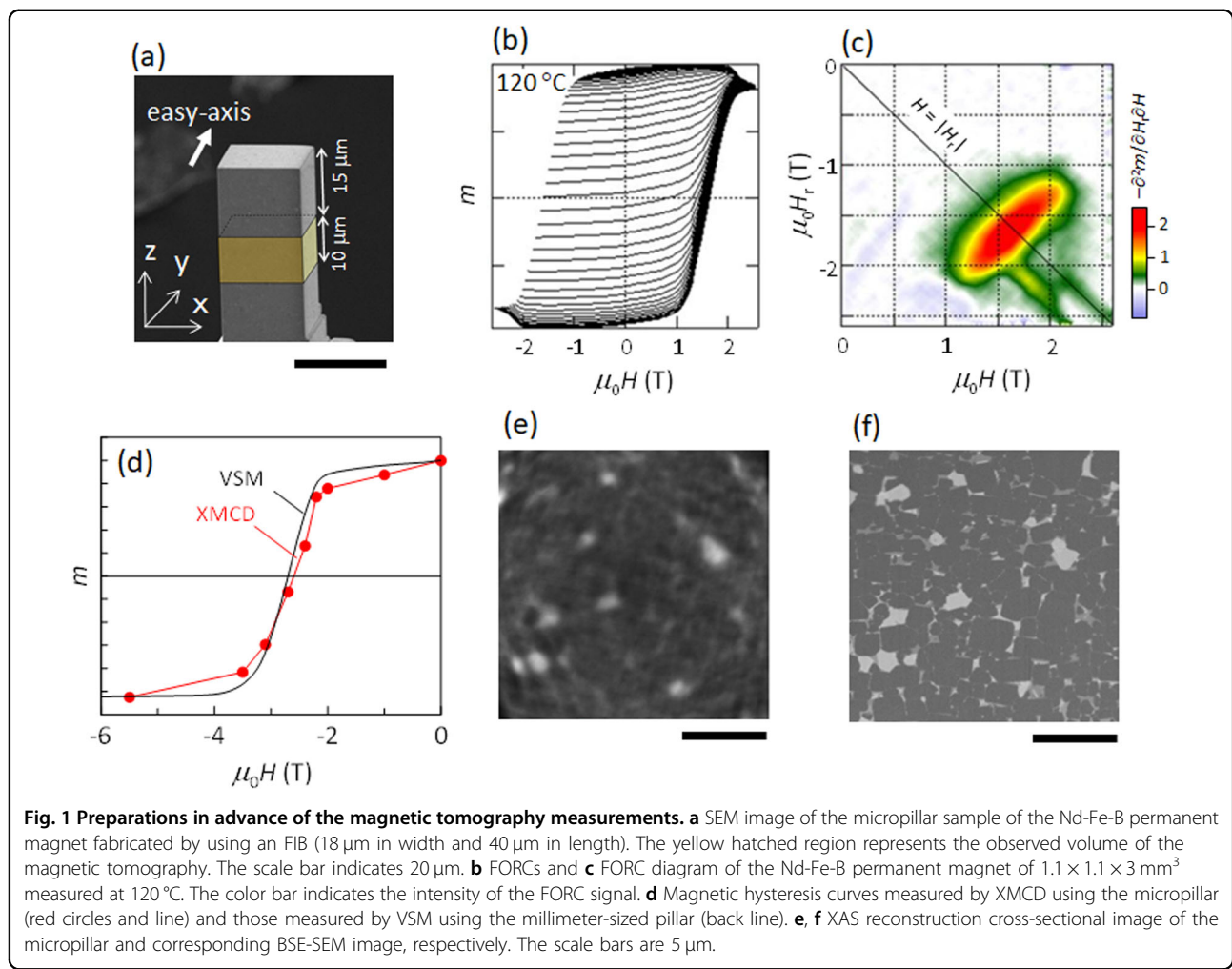


Fig. 1 Preparations in advance of the magnetic tomography measurements. **a** SEM image of the micropillar sample of the Nd-Fe-B permanent magnet fabricated by using an FIB (18 μm in width and 40 μm in length). The yellow hatched region represents the observed volume of the magnetic tomography. The scale bar indicates 20 μm. **b** FORCs and **c** FORC diagram of the Nd-Fe-B permanent magnet of $1.1 \times 1.1 \times 3$ mm 3 measured at 120 °C. The color bar indicates the intensity of the FORC signal. **d** Magnetic hysteresis curves measured by XMCD using the micropillar (red circles and line) and those measured by VSM using the millimeter-sized pillar (black line). **e, f** XAS reconstruction cross-sectional image of the micropillar and corresponding BSE-SEM image, respectively. The scale bars are 5 μm.

corresponds to the sample area was extracted with a size of $17.8 \times 17.8 \times 9.8$ μm 3 and processed by FFT without a window function. The resulting resolution in reciprocal space was $\Delta q_x = \Delta q_y = 0.056$ μm $^{-1}$ and $\Delta q_z = 0.10$ μm $^{-1}$.

Results and discussion

Magnetic tomography experiment

The magnet sample was microfabricated into a rectangular pillar (18 μm in width and 40 μm in length), as shown in Fig. 1a. The *c*-axis of each Nd₂Fe₁₄B grain, which is the easy magnetization axis, was aligned along the short axis of the pillar, and the magnetic field was applied in this direction. This direction is referred to as the *easy axis* in this study. Before the magnetic tomography measurement, the magnetization reversal behavior of a larger pillar sample of 1.1 mm in width and 3 mm in length (easy axis along the short axis) was investigated using the first-order reversal curve (FORC) measurement^{34,39–42}. Figure 1b shows the FORCs measured using a vibrating sample magnetometer (VSM). The FORC measurement was performed at an elevated temperature of 120 °C to saturate the sample under a maximum field of

2.6 T generated from the electromagnet of the VSM system. The FORCs represent the magnetization curves with the magnetic field H starting from H_r on the major magnetic hysteresis curve. The major magnetic hysteresis loop is filled with FORCs by varying H_r from zero to negative saturation. Then, the FORC diagram shown in Fig. 1c was obtained by plotting the second-order differentiated magnetization with respect to H and H_r . A perpendicularly prolonged pattern is observed on the downward diagonal line of $H = |H_r|$. This is a typical pattern for a narrow coercivity distribution with a large interaction field^{41,42}, which corresponds to the short-axis demagnetization field $\mu_0 N_x M_s \approx 0.5$ T, where μ_0 , N_x , and M_s represent the permeability in vacuum, demagnetization factor along the short-axis, and saturation magnetization, respectively. Furthermore, the tail in the high-field region along the line of $H = |H_r|$ was found, indicating the existence of unsaturated grains in the high-field region, which is considerably larger than the coercivity⁴¹.

The magnetic tomography measurement was performed using a focused hard X-ray beam at an X-ray energy of the Nd *L*₂ edge at BL39XU of SPring-8. The observed volume

is a 10 μm height region located 15 μm from the tip of the micropillar, as shown in Fig. 1a. Thus, the observed volume is estimated to contain ~ 4000 grains. This large number of grains within the observed volume is sufficient to reproduce the real magnetic domain behavior in bulk Nd-Fe-B sintered magnets.

The micropillar sample was set into an external electro- or superconducting magnet for applying a magnetic field. The sample was then mounted on a magnetic tomography measurement setup. Next, the measurement was performed for the magnetic remanent state of the sample, and this process was repeated by changing the external magnetic field. After finishing all magnetic tomography measurements, microstructure tomography was carried out by sequentially recording the scanning electron microscopy (SEM) of backscattered electron (BSE) images while slicing the sample using a Ga-ion FIB³⁶.

Figure 1d shows the integrated XMCD signal for the observed volume as a function of the external magnetic field H , which corresponds to the averaged magnetization in the volume. The magnetic hysteresis curve of the millimeter-sized sample is also plotted as the black solid line, which was obtained by applying a maximum external magnetic field of 14 T using a VSM with a superconducting magnet. XMCD integration was performed for the volume excluding the outermost surface of 1 μm thickness because the outermost surface grains of the micropillar lose their hard magnetic properties attributed to FIB damage. Therefore, the XMCD curve of the micropillar agrees with the magnetic hysteresis curve of the millimeter-sized sample, indicating that the magnetic domain structure of the micropillar observed by XMCD is unaffected by the surface and well represents that of the bulk magnet.

The reconstructed X-ray absorption (XAS) image of the cross-sectional plane of the micropillar is shown in Fig. 1e. The white spots in the XAS image are non-magnetic Nd-rich phases, such as metallic Nd, fcc-NdO, and Nd₂O₃³⁶, because the XAS image corresponds to the Nd density distribution. The corresponding plane of the BSE-SEM image can be precisely identified by utilizing these Nd-rich regions of the XAS image as 3D position markers (see Supplementary Video 1), as shown in Fig. 1f. In addition to these white spots, many wavy obscured patterns were observed in the XAS image. Some of them correspond to the Nd-rich regions seen in the BSE-SEM image in Fig. 1f; however, some uncorrelated patterns remain due to the artifacts in tomographic reconstruction from the limited number of projections and the weak transmitted X-ray intensity passing through the relatively thick sample (25 μm in a diagonal direction).

3D magnetic images are reconstructed from the measured XMCD projection images by a scalar magnetic tomographic reconstruction, which represents the

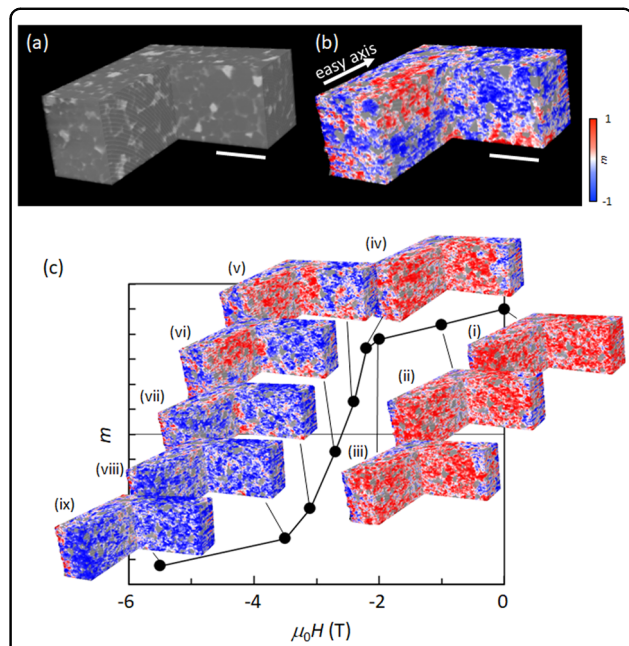


Fig. 2 Microstructure and magnetic tomography experimental results. **a, b** Cut-away 3D BSE-SEM and magnetic images, respectively. The scale bars are 5 μm . **c** Cut-away 3D magnetic images along the magnetic hysteresis curve. Gray regions in 3D magnetic images are nonmagnetic Nd-rich phases from binarized SEM images. The color bar indicates the normalized magnetization m .

distribution of a magnetic vector component parallel to the easy axis. Figure 2a, b show the cutaway 3D BSE-SEM and magnetic images observed from the same region, respectively. A 1 μm thick surface rim of the sample was excluded. The gray regions in the magnetic image are the binarized nonmagnetic Nd-rich regions from the BSE-SEM image. In the 3D magnetic image, the domain structure is observed clearly as red and blue regions for the positive and negative magnetizations along the easy axis, although randomly distributed white ghost patterns are seen. Figure 2c shows the cutaway 3D magnetic images at different external fields $\mu_0 H$ along with the magnetic hysteresis curve starting from positive saturation to negative saturation; the details are presented in Supplementary Fig. S4. The reversed domains appear from the edges at $\mu_0 H = -1$ T (Fig. 2c, (ii)) because of the damaged soft magnetic surface layer. The areal fraction of the reversed domains increases gradually with decreasing external magnetic field, but they stay located at the edges until $\mu_0 H = -2.2$ T (Fig. 2c, (iv)). Then, the reversed domains largely expand at $\mu_0 H = -2.4$ T (Fig. 2c, (v)) and approach negative saturation. The existence of unreversed grains can be confirmed near negative saturation (Fig. 2c, (vii), and (viii)), which is expected from the FORC diagram measurement (Fig. 1c).

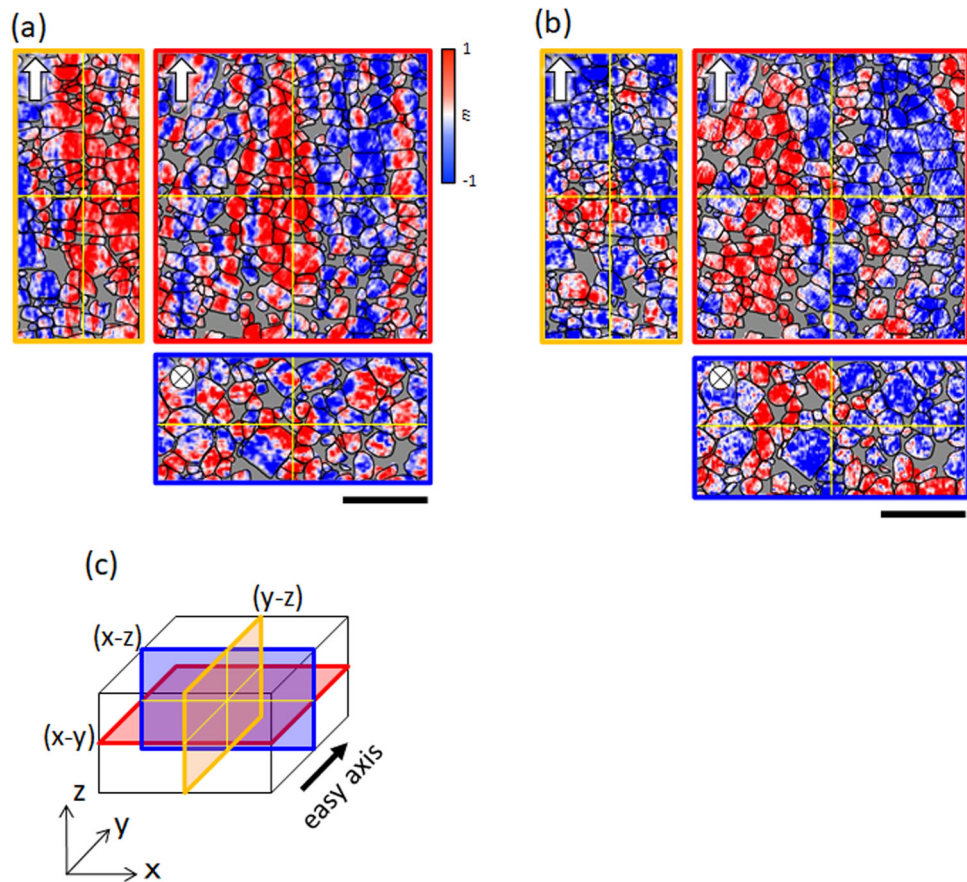


Fig. 3 3D cross-sectional images of the micropillar Nd-Fe-B permanent magnet sample. **a, b** Thermally demagnetized state and coercivity state at $\mu_0H = -2.7$ T, respectively. White arrows and white circles with crosses indicate the easy axis directions on each plane, and the black lines are the grain boundaries drawn from the corresponding 3D cross-sectional BSE-SEM images. Red, yellow, and blue frames of each image correspond to the cross-sectional planes of (x-y), (y-z), and (x-z), respectively, as schematically shown in **c**. Thin yellow lines indicate the intersections of the (x-y), (y-z), and (x-z) planes. The color bar indicates the normalized magnetization m . The scale bar is 5 μm .

Magnetic domain structures of thermally demagnetized and coercivity states

Figure 3a, b show the cross-sectional 3D magnetic images for the thermally demagnetized and coercivity states ($\mu_0H = -2.7$ T), respectively. The red, yellow, and blue frame colors correspond to the (x-y), (y-z), and (x-z) cross-sectional planes, respectively, as schematically shown in Fig. 3c. Although both the thermally demagnetized and coercivity states are macroscopically demagnetized, their microscopic domain structures are considerably different. Stripe domains are clearly found along the easy axis with a width of $2 \sim 4$ grains for the thermally demagnetized state. The domain walls run straight, irrespective of the grain boundary. On the other hand, large and irregular domains are found in the coercivity state, and their domain walls are pinned at the grain boundary.

In general, these domain structures, i.e., straight stripe domains in the thermally demagnetized state and large domains in the coercivity state, reflect the intergrain

exchange and magnetostatic interactions existing in the magnet. Micromagnetics simulation based on the Landau-Lifschitz-Gilbert equation was performed to calculate the domain structure of the thermally demagnetized state with and without the intergrain exchange interaction, as shown in Supplementary Fig. S5. As a result, both magnetic domain structures are similar, indicating that the magnetostatic interaction is the major role for the straight stripe domains in the thermally demagnetized state. On the other hand, the large domains observed in the coercivity state suggest the existence of nonnegligible intergrain exchange interactions even in the advanced coercivity Nd-Fe-B sintered magnet¹⁵.

Fourier transformation analysis was performed to examine the characteristic features of the 3D magnetic domain structure. Figure 4a, b compare the fast Fourier transform (FFT) spectra of the 3D magnetic images of the thermally demagnetized and coercivity states ($\mu_0H = -2.7$ T), respectively, where $\mathbf{q} = (q_x, q_y, q_z)$ represents a wavenumber vector

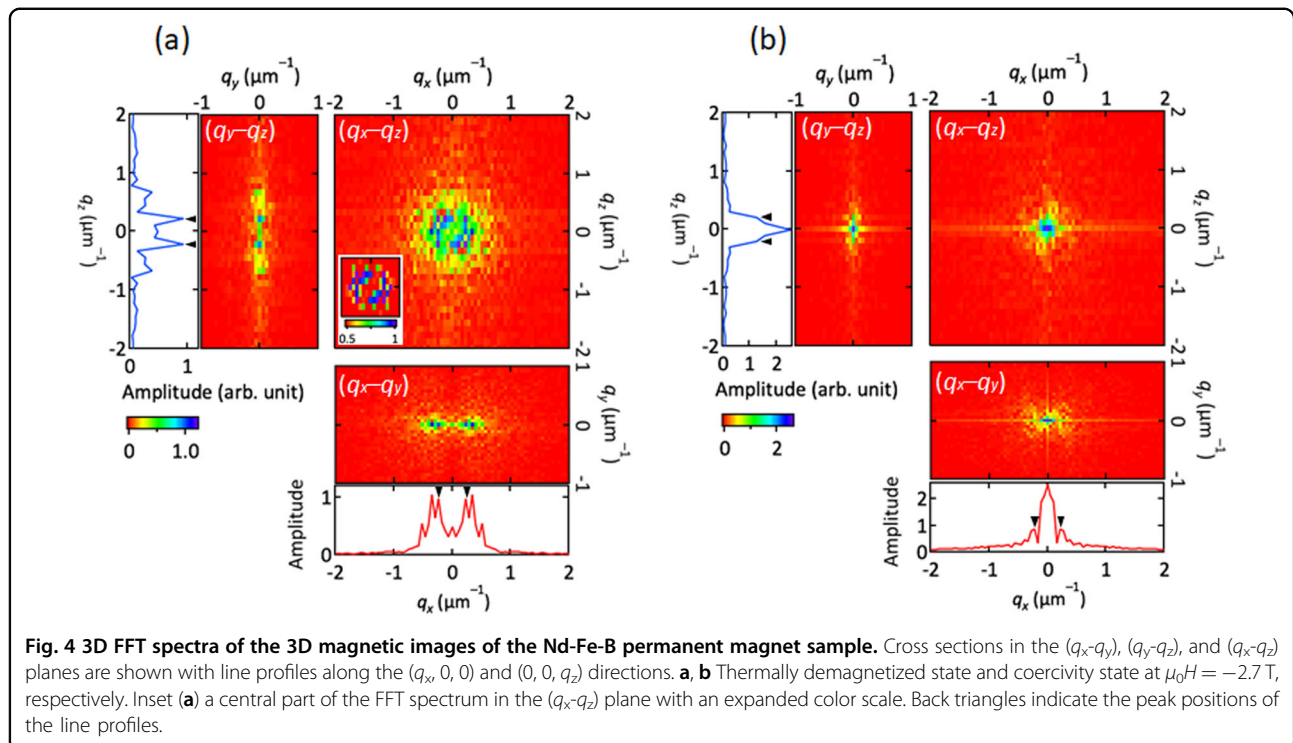


Fig. 4 3D FFT spectra of the 3D magnetic images of the Nd-Fe-B permanent magnet sample. Cross sections in the (q_x-q_y) , (q_y-q_z) , and (q_x-q_z) planes are shown with line profiles along the $(q_x, 0, 0)$ and $(0, 0, q_z)$ directions. **a, b** Thermally demagnetized state and coercivity state at $\mu_0 H = -2.7$ T, respectively. Inset (a) a central part of the FFT spectrum in the (q_x-q_z) plane with an expanded color scale. Back triangles indicate the peak positions of the line profiles.

in reciprocal space. These FFT spectra correspond to spin-polarized small-angle neutron scattering (SP-SANS) spectra⁴³. The SP-SANS spectra include both the magnetic and structural information, whereas the FFT spectra in Fig. 4, calculated from the 3D magnetic domain images, comprise magnetic information only. The thermally demagnetized state (Fig. 4a) exhibits the 3D FFT spectra of a thin doughnut-like pattern that lies in the (q_x-q_z) plane, with the main Fourier components confined to the region of $|q_y| < 0.2 \mu\text{m}^{-1}$. In the inset of Fig. 4a shown with an expanded color scale, the doughnut shape with a radius of $|\mathbf{q}| \sim 0.25 \mu\text{m}^{-1}$ is more visible. These spectra reflect the stripe domain structure extending along the y -axis (easy axis), as indicated in Fig. 3a. Prominent peak structures at $\mathbf{q} = (\pm 0.22 \mu\text{m}^{-1}, 0, 0)$ in the (q_x-q_y) plane and at $\mathbf{q} = (0, 0, \pm 0.22 \mu\text{m}^{-1})$ in the (q_y-q_z) planes correspond to the magnetic structure with a mean half-period of $2.3 \mu\text{m}$, which is the magnetic domain width. The coercivity state (Fig. 4b) shows the 3D FFT spectra with a strong component concentrated at the origin in the region of $|q_x|, |q_y|, |q_z| < 0.15 \mu\text{m}^{-1}$. The spectrum with strong low-frequency components indicates the formation of a large and less periodic magnetic domain structure of the coercivity state, as shown in Fig. 3b. However, Fig. 4b shows that there are side-band peaks at $\mathbf{q} = (\pm 0.22 \mu\text{m}^{-1}, 0, 0)$ and $(0, 0, \pm 0.22 \mu\text{m}^{-1})$, which are similar to those in the demagnetized state. This fact indicates that the magnetic domain structure of the coercivity state is weakly modulated with the same periodicity as in the thermally demagnetized state. The above analysis suggests that

the reciprocal vector component of the magnetic structure $\mathbf{q}_{x-z} = (q_x, 0, q_z)$ with $|\mathbf{q}_{x-z}| = \sqrt{q_x^2 + q_z^2} = 0.22 \mu\text{m}^{-1}$ is determined as the characteristic length of $2.3 \mu\text{m}$ of this magnetic domain irrespective of the magnetization states.

Local magnetic domain behaviors

Some interesting local magnetic domain behaviors were observed from the careful examination of the 3D magnetic domain structure. One is the intrinsic nucleation and annihilation of magnetic domains inside the permanent magnet. In conventional 2D magnetic domain observations, similar nucleation and annihilation of magnetic domains have already been observed¹⁵. However, these observations could be the tips of large domains existing underneath the surface, and there is no method to distinguish them from the 2D magnetic domain observations using MOKE microscopy. Figure 5a, b show the real nucleation and annihilation of magnetic domains experimentally observed for the first time. The surrounding areas were dimmed to highlight the grains of interest. At $\mu_0 H = -2.2$ T (Fig. 5a), where the shoulder of the magnetic hysteresis curve appears, a reversed grain exists in isolation from the other reversed domains. This grain has a prolate shape, and the long axis is tilted from the easy axis on the $(y-z)$ plane. The short axis of the grain is considered to be parallel to the c -axis because $\text{Nd}_2\text{Fe}_{14}\text{B}$ grains preferentially grow perpendicular to the c -axis⁴⁴. This finding indicates that the grain with a tilted c -axis

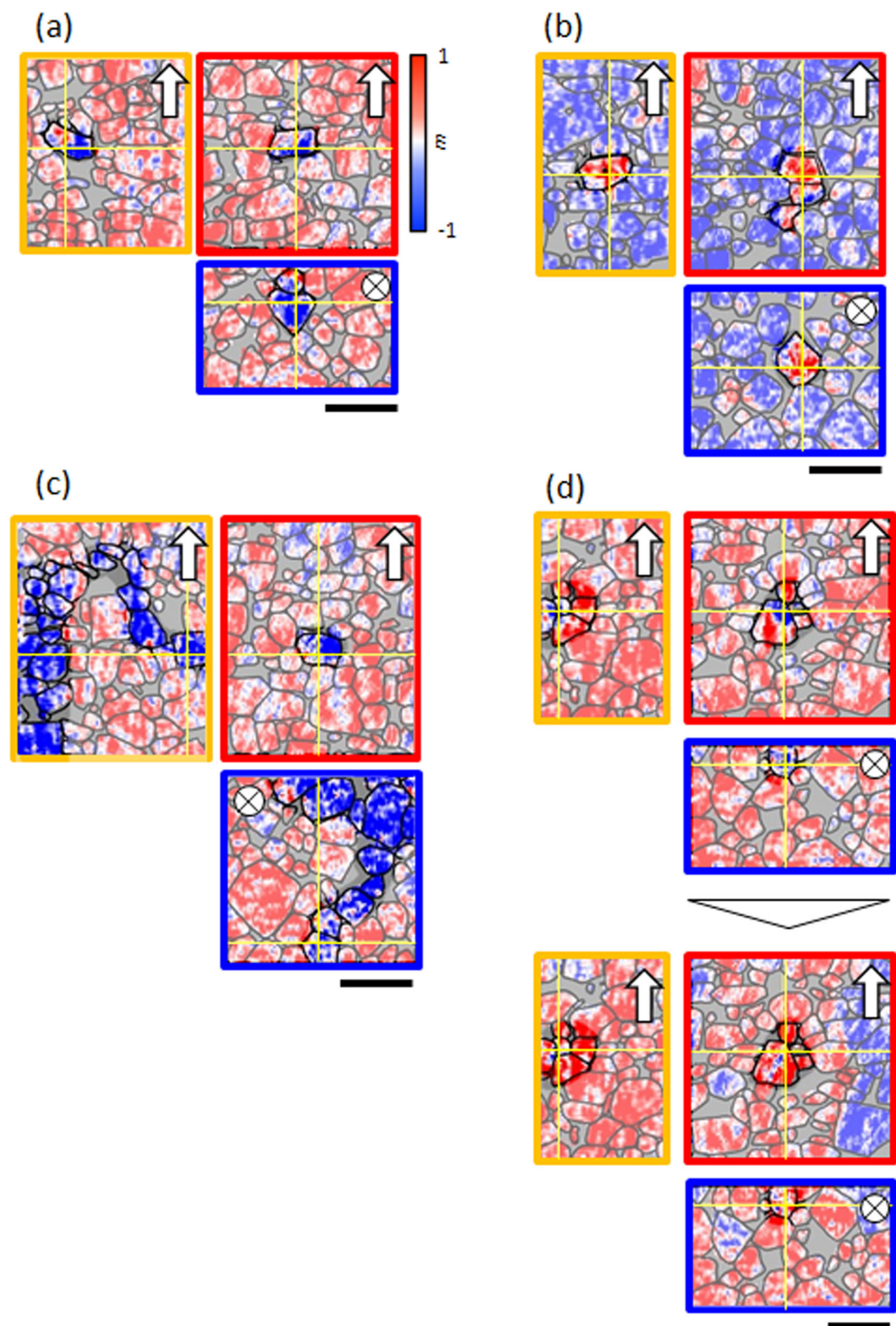


Fig. 5 (See legend on next page.)

(see figure on previous page)

Fig. 5 3D cross-sectional images of the detailed features of magnetic domain behaviors along magnetic hysteresis. **a** Nucleation site of the reversed domain found at $\mu_0H = -2.2$ T. **b** Annihilation site of the unreversed magnetic domain found at $\mu_0H = -3.5$ T. **c** Magnetic domain running perpendicular to the easy axis on the (x-z) plane found at $\mu_0H = -2.4$ T. **d** Grain that reverses its magnetization at $\mu_0H = -2.2$ T (upper) and reverses them back at $\mu_0H = -2.4$ T (lower) against the magnetic field. White arrows and white circles with the cross indicate the easy axis directions on each plane, and the black lines are the grain boundaries drawn from the corresponding 3D cross-sectional BSE-SEM images. The red, yellow, and blue frames of each image correspond to the cross-sectional planes of (x-y), (y-z), and (x-z), respectively, as schematically shown in Fig. 3c. The surrounding regions are dimmed to highlight the grains of interest. Thin yellow lines indicate the intersections of the (x-y), (y-z), and (x-z) planes. The color bars indicate the normalized magnetization m . The scale bars are 3 μm .

would be the nucleation site, as discussed by the micromagnetic simulations²². At $\mu_0H = -3.5$ T (Fig. 5b), which is close to the negative saturation of the magnetic hysteresis curve, an unreversed row of three grains is observed, which also exists in isolation from the other unreversed domains. This is the intrinsic annihilation site of the unreversed domain.

We also observed unexpected local magnetic domain behaviors. Figure 5c shows a reversed magnetic grain chain found at $\mu_0H = -2.4$ T. This reversed grain chain bends on the (y-z) plane. Surprisingly, this grain chain on the (x-z) plane runs perpendicular to the easy axis, whereas the magnetization of each grain aligns along the easy axis. This magnetization state is energetically unfavorable because of the strong magnetostatic interaction field along the grain chain. This finding suggests the existence of a locally strong anisotropic intergrain exchange interaction perpendicular to the c -axis to compensate for the magnetostatic interaction field. Such an anisotropic feature of the grain boundary phases was reported in Nd-Fe-B sintered magnets^{33,45}.

Figure 5d shows the existence of a grain in which the magnetization reverses back against the magnetic field. The upper cross-sectional 3D magnetic images at $\mu_0H = -2.2$ T show partially reversed grains. The reversed domain seems to come from the outer upper region of the observation area because the left and upper sides of the (y-z) and (x-z) planes, respectively, are the top end of the observation region. This reversed domain largely shrinks on the lower cross-sectional 3D magnetic images at $\mu_0H = -2.4$ T near the coercivity. Near the coercivity, the reversed magnetic domains largely expanded, as shown in Fig. 2 and Supplementary Fig. S4, with decreasing magnetic field, which caused a significant change in the local magnetostatic interaction field. Thus, it is plausible that this unnatural magnetic domain behavior is a consequence of the reformation of the magnetic domain structure attributed to the large change in the local magnetostatic interaction field.

Summary

We demonstrated the first 3D observation of magnetic domain behaviors of a bulk permanent magnet using hard X-ray MCD tomography with high field electro- and

superconducting magnets. The 3D magnetic domain structure was precisely correlated with the 3D microstructure tomography image obtained from the same volume. The 3D magnetic domain structure dynamics were successfully visualized along the magnetic hysteresis curve. This technique opens up a new stage of permanent magnet study. The characteristic lengths of the thermally demagnetized and coercivity states were evaluated from the FFT analysis, and some unexpected local magnetic domain behaviors were observed. More detailed characteristic features of magnetic domain dynamics can be revealed from the 3D magnetic domain observation method with more statistical analysis, including machine learning technologies. Enhancing the signal intensity and throughput in magnetic tomography measurements are the next challenges for this purpose and for time-resolved 3D microscopy of magnetization dynamics in permanent magnets in the future.

Acknowledgements

We gratefully thank S. Hirosawa, S. Miyashita, and T. Iriyama for their fruitful discussions, Y. Toyooka for the Tb-Cu grain boundary diffusion process, J. Uzuhashi for the scanning electron microtomography measurements, and R. Kamamoto for image processing. FIB patterning was performed at the Material Solution Center (MaSC), Tohoku University, with great support from K. Sato. This work was partially supported by the Elements Strategy Initiative Center for Magnetic Materials (ESICMM), Grant Number JPMXP0112101004, through the Ministry of Education, Culture, Sports, Science and Technology (MEXT), and the Research Program of "Five-Star Alliance" in "NJRC Mater. & Dev.". The magnetic tomography experiments were performed at BL39XU, Spring-8, with the approval of the Japan Synchrotron Radiation Research Institute (JASRI) (Proposal Nos. 2018A1129, 2018A2067, 2018B1015, 2018B1332, 2018B2100, 2019A1555, 2019B1003, 2020A0816, and 2020A1005).

Author details

¹Institute of Multidisciplinary Research for Advanced Materials (IMRAM), Tohoku University, Sendai 980-8577, Japan. ²Kwansei Gakuin University, Sanda 669-1330, Japan. ³Japan Synchrotron Radiation Research Institute (JASRI), Sayo 679-5198, Japan. ⁴Elements Strategy Initiative Center for Magnetic Materials (ESICMM), National Institute for Materials Science (NIMS), Tsukuba 305-0047, Japan. ⁵International Center for Synchrotron Radiation Innovation Smart, (SRIS), Tohoku University, Sendai 980-8577, Japan. ⁶Center for Spintronics Research Network (CSR), Tohoku University, Sendai 980-8577, Japan. ⁷Daido Steel Co., Ltd, Nagoya 461-8581, Japan

Author contributions

S.O. and M.S. designed and managed the research project; M.T. and N.K. fabricated the micropillar samples and performed magnetic characterizations; Y.U. prepared the advanced permanent magnet sample; M.T., S.K., Y.K., M.S., and S.O. performed the magnetic tomography experiments; H.A. and A.B. conducted the micromagnetic calculations; T.O. and K.H. managed the microstructure tomography experiments; M.S., M.T., T.N., and S.O. analyzed the

data; and S.O. and M.S. drafted the paper. All authors discussed the results and commented on the manuscript.

Conflict of interest

The authors declare no competing interests.

Publisher's note

Springer Nature remains neutral with regard to jurisdictional claims in published maps and institutional affiliations.

Supplementary information The online version contains supplementary material available at <https://doi.org/10.1038/s41427-022-00417-0>.

Received: 16 March 2022 Revised: 27 June 2022 Accepted: 28 June 2022.

Published online: 19 August 2022

References

1. Honda, K. TOKUSHU-GOUKIN-KOU (in Japanese), Japan Patent 32234 (1917).
2. Strnat, K. The recent development of permanent magnet materials containing rare earth metals. *IEEE Trans. Magn.* **MAG-6**, 182–190 (1970).
3. Herbst, J. F. $R_2Fe_{14}B$ materials: intrinsic properties and technological aspects. *Rev. Mod. Phys.* **63**, 819–898 (1991).
4. Coey, J. M. D. Hard magnetic materials: a perspective. *IEEE Trans. Magn.* **47**, 4671–4681 (2011).
5. Sugimoto, S. Current status and recent topics of rare-earth permanent magnets. *J. Phys. D Appl. Phys.* **44**, 064001 (2011).
6. Hono, K. & Sepehri-Amin, H. Strategy for high-coercivity Nd–Fe–B magnets. *Scr. Mater.* **67**, 530–535 (2012).
7. Livingston, J. D. Magnetic domains in sintered Fe–Nd–B magnets. *J. Appl. Phys.* **57**, 4137–4139 (1985).
8. Mishra, R. K. Microstructure of melt-spun Nd–Fe–B magnequench magnets. *J. Magn. Magn. Mater.* **54–57**, 450–456 (1986).
9. Folks, L., Street, R., Woodward, R. C. & Babcock, K. Magnetic force microscopy images of high-coercivity permanent magnets. *J. Magn. Magn. Mater.* **159**, 109–118 (1996).
10. Gutfleisch, O., Eckert, D., Schafer, R., Muller, K. H. & Panchanathan, V. Magnetization processes in two different types of anisotropic, fully dense NdFeB hydrogenation, disproportionation, desorption, and recombination magnets. *J. Appl. Phys.* **87**, 6119–6121 (2000).
11. Shinba, Y., Konno, T. J., Ishikawa, K., Hiraga, K. & Sagawa, M. Transmission electron microscopy study on Nd-rich phase and grain boundary structure of Nd–Fe–B sintered magnets. *J. Appl. Phys.* **97**, 053504 (2005).
12. Kohashi, T., Motai, K., Nishiuchi, T., Maki, T. & Hirosawa, S. Analysis of mechanism for NdFeB magnet using spin-polarized scanning electron microscopy (spin SEM). *J. Magn. Soc. Jpn.* **33**, 374–378 (2009).
13. Ono, K. et al. Element-specific magnetic domain imaging of (Nd, Dy)–Fe–B sintered magnets using scanning transmission X-ray microscopy. *IEEE Trans. Magn.* **47**, 2672–2675 (2011).
14. Takezawa, M., Ogimoto, H., Kimura, Y. & Morimoto, Y. Analysis of the demagnetization process of Nd–Fe–B sintered magnets at elevated temperatures by magnetic domain observation using a Kerr microscope. *J. Appl. Phys.* **115**, 17A733 (2014).
15. Soderžnik, M. et al. Magnetization reversal of exchange-coupled and exchange-decoupled Nd–Fe–B magnets observed by magneto-optical Kerr effect microscopy. *Acta Mater.* **135**, 68–76 (2017).
16. Suzuki, M. et al. Magnetic domain evolution in Nd–Fe–BCu sintered magnet visualized by scanning hard X-ray microprobe. *Acta Mater.* **106**, 155–161 (2016).
17. Billington, D. et al. Unmasking the interior magnetic domain structure and evolution in Nd–Fe–B sintered magnets through high-field magnetic imaging of the fractured surface. *Phys. Rev. Mater.* **2**, 104413 (2018).
18. Schrefl, T., Roitner, H. & Fidler, J. Dynamic micromagnetics of nanocomposite NdFeB magnets. *J. Appl. Phys.* **81**, 5567–5569 (1997).
19. Fujisaki, J. et al. Micromagnetic simulations of magnetization reversal in misaligned multigrain magnets with various grain boundary properties using large-scale parallel computing. *IEEE Trans. Magn.* **50**, 7100704 (2014).
20. Sepehri-Amin, H., Ohkubo, T. & Hono, K. Micromagnetic simulations of magnetization reversals in Nd–Fe–B based permanent magnets. *Mater. Trans.* **57**, 1221–1229 (2016).
21. Westmoreland, S. C. et al. Multiscale model approaches to the design of advanced permanent magnets. *Scr. Mater.* **148**, 56–62 (2018).
22. Tsukahara, H., Iwano, K., Ishikawa, T., Mitsumata, C. & Ono, K. Large-scale micromagnetics simulation of magnetization dynamics in a permanent magnet during the initial magnetization process. *Phys. Rev. Appl.* **11**, 014010 (2019).
23. Manke, I. et al. Three-dimensional imaging of magnetic domains. *Nat. Commun.* **1**, 125 (2010).
24. Hierro-Rodríguez, A. et al. Revealing 3D magnetization of thin films with soft X-ray tomography: Magnetic singularities and topological charges. *Nat. Commun.* **11**, 6382 (2020).
25. Donnelly, C. et al. Three-dimensional magnetization structures revealed with X-ray vector tomography. *Nature* **547**, 328–331 (2017).
26. Suzuki, M. et al. Three-dimensional visualization of magnetic domain structure with strong uniaxial anisotropy via scanning hard X-ray microtomography. *Appl. Phys. Express* **11**, 036601 (2018).
27. Donnelly, C. et al. Time-resolved imaging of three-dimensional nanoscale magnetization dynamics. *Nat. Nanotechnol.* **15**, 356–360 (2020).
28. Suzuki, M. et al. Magnetic microscopy using a circularly polarized hard X-ray nanoprobe at SPring-8. *Synch. Rad. N.* **33**, 4–11 (2020).
29. Seki, S. et al. Direct visualization of the three-dimensional shape of skyrmion strings in a noncentrosymmetric magnet. *Nat. Mater.* **21**, 181–187 (2022).
30. Sagawa, M., Fujimura, S., Togawa, N., Yamamoto, H. & Matsuu, Y. New material for permanent magnets on a base of Nd and Fe. *J. Appl. Phys.* **55**, 2083–2087 (1984).
31. Croat, J. J., Herbst, J. F., Lee, R. W. & Pinkerton, F. E. High-energy product Nd–Fe–B permanent magnets. *Appl. Phys. Lett.* **44**, 148–149 (1984).
32. Gutfleisch, O. et al. Magnetic materials and devices for the 21st century: Stronger, lighter, and more energy efficient. *Adv. Mater.* **23**, 821–842 (2011).
33. Sasaki, T. T., Ohkubo, T. & Hono, K. Structure and chemical compositions of the grain boundary phase in Nd–Fe–B sintered magnets. *Acta Mater.* **115**, 269–277 (2016).
34. Miyazawa, K. et al. First-order reversal curve analysis of a Nd–Fe–B sintered magnet with soft X-ray magnetic circular dichroism microscopy. *Acta Mater.* **162**, 1–9 (2019).
35. Sasaki, T. T. et al. Formation of non-ferromagnetic grain boundary phase in a Ga-doped Nd-rich Nd–Fe–B sintered magnet. *Scr. Mater.* **113**, 5218–5221 (2016).
36. Sepehri-Amin, H., Une, Y., Ohkubo, T., Hono, K. & Sagawa, M. Microstructure of fine-grained Nd–Fe–B sintered magnets with high coercivity. *Scr. Mater.* **65**, 396–399 (2011).
37. Une, Y. & Sagawa, M. Enhancement of coercivity of Nd–Fe–B sintered magnets by grain size reduction. *J. Jpn. Inst. Met. Mater.* **76**, 12–16 (2012), in Japanese.
38. Li, J. et al. Coercivity and its thermal stability of Nd–Fe–B hot-deformed magnets enhanced by the eutectic grain boundary diffusion process. *Acta Mater.* **161**, 171–181 (2018).
39. Mayergoyz, I. D. Mathematical models of hysteresis. *IEEE Trans. Magn.* **22**, 603–608 (1986).
40. Okamoto, S. et al. Temperature-dependent magnetization reversal process of a Ga-doped Nd–Fe–B sintered magnet based on first-order reversal curve analysis. *Acta Mater.* **178**, 90–98 (2019).
41. Yomogita, T. et al. Temperature and field direction dependences of first-order reversal curve (FORC) diagrams of hot-deformed Nd–Fe–B magnets. *J. Magn. Magn. Mater.* **447**, 110–115 (2018).
42. Pike, C. R., Roberts, A. P. & Verosub, K. L. Characterizing interactions in fine magnetic particle systems using first-order reversal curves. *J. Appl. Phys.* **85**, 6660–6667 (1999).
43. Yano, M. et al. Magnetic reversal observation in nanocrystalline Nd–Fe–B magnet by SANS. *IEEE Trans. Magn.* **48**, 2804–2807 (2012).
44. Tenaud, P. et al. Texture in Nd–Fe–B magnets analysed on the basis of the determination of $Nd_2Fe_{14}B$ single crystals easy growth axis. *Solid State Commun.* **63**, 303–305 (1987).
45. Xu, X. D. et al. Microstructure of a Dy-free Nd–Fe–B sintered magnet with 2T coercivity. *Acta Mater.* **156**, 146–157 (2018).